Strongly Enhanced Second Harmonic Generation in a Thin Film Lithium Niobate Heterostructure Cavity

Shuai Yuan,[1,*] Yunkun Wu,[2,3,*] Zhongzhou Dang,[1] Cheng Zeng,[1] Xiaozhuo Qi,[2,3] Guangcan Guo,[2,3] Xifeng Ren,[2,3,†] and Jinsong Xia[1,‡]

[1]*Wuhan National laboratory of Optoelectronics, Huazhong University of Science and Technology, Wuhan 430074, China*
[2]*Key Laboratory of Quantum Information, CAS, University of Science and Technology of China, Hefei 230026, China*
[3]*Synergetic Innovation Center of Quantum Information and Quantum Physics, University of Science and Technology of China, Hefei, Anhui 230026, China*

(Received 26 April 2021; accepted 31 August 2021; published 6 October 2021)

Boosting second-order optical nonlinear frequency conversion over subwavelength thickness has long been pursued through optical resonance in micro- and nanophotonics. However, the availability of thin film materials with high second-order nonlinearity is limited to III-V semiconductors, which have low transparency in the visible. Here, we experimentally demonstrated strongly enhanced second harmonic generation in one-dimensional heterostructure cavities on thin film lithium niobate. A guided-mode resonance resonator and distributed Bragg reflectors are combined for both efficient coupling and electromagnetic field localization. Over 1200 times second harmonic generation enhancement is experimentally realized compared with flat thin film lithium niobate through optimizing the trade-off between quality factor and mode volume, leading to a record high normalized conversion efficiency of 2.03×10^{-5} cm^2/GW under 1.92 MW/cm^2 pump intensity. Our approach could inspire the miniaturization and integration of compact resonant nonlinear photonic devices on thin film lithium niobate.

DOI: 10.1103/PhysRevLett.127.153901

Lithium niobate [$LiNbO_3$ (LN)] has been regarded as the key material in optics because of its excellent optical properties [1–5]. In recent years, the successful fabrication of submicrometer-thickness single-crystal LN on a low-index substrate has started a new platform of "lithium niobate on insulator" (LNOI) [6–8]. The high-index contrast of LNOI and the recently developed micro- and nanostructuring techniques enable the fabrication of subwavelength LNOI waveguide devices. Till now, LNOI is emerging as an important material platform for photonics and optoelectronic systems, with a variety of high-performance devices demonstrated on it—for instance, an ultrahigh-speed electro-optic modulator operating at low voltages [9–12]; high-efficiency nonlinear generation devices based on periodically poled LN [13–15]; photonic crystal [16–18], microdisks [19,20], and ring resonators [21,22]; and a broadband frequency comb system [23,24].

In particular, the high second-order nonlinearity $\chi^{(2)}$ and wide transparency window of LN make it the ideal material for second-order nonlinear optical interactions, including second harmonic generation (SHG) [25–27], sum frequency generation [28,29], and difference frequency generation [30]. To enhance nonlinear processes in LNOI waveguides, the quasi-phase-matching method has been used to compensate the phase velocity mismatch [14]. A gradient metasurface was employed to realize phase-matching free wavelength conversion in a LNOI waveguide [26]. In addition, a high quality factor (Q factor) photonic crystal cavity has been used for phase-matching free SHG in the subwavelength dimension [17]. Considering the field enhancement in optical resonant structure and convenient free space coupling, resonant metasurface [31,32], guided resonance resonators, and dielectric loaded resonators [33] based on LNOI have also been proposed. A Q factor around 10 and several times enhancement of the SHG efficiency were realized on LN metasurface at visible wavelengths [34], which are yet to be improved. Therefore, experimental demonstration of larger enhancement of SHG for resonant LNOI structures is of paramount importance, which could be achieved under a higher Q factor and stronger optical field confinement, as the nonlinear interaction strength is proportional to the light intensity inside the structure.

For decades, guided-mode-resonance (GMR) resonators have been intensively studied due to the optical field enhancement and convenient free space excitation [35–40]. With proper design of the structure parameters, high-Q optical resonance at the Γ point (corresponding to normal incidence) can be realized. Especially, in the situation of a GMR resonator composed of only a few cycles, strong field localization and enhancement could be realized in combination with photonic band-gap structure like a distributed Bragg reflector (DBR), forming a heterostructure cavity. These characteristics make the GMR resonator a best candidate to achieve high-efficiency nonlinear frequency

conversion in thin film materials under free space excitation.

In this Letter, we experimentally demonstrate strongly enhanced SHG efficiency from nonlinear GMR heterostructure cavities on LNOI. The device is fabricated on x-cut LNOI thin films using electron beam lithography (EBL) and inductively coupled plasma (ICP) etching. Because of the strong optical field confinement provided by DBR on both sides of the one-dimensional GMR resonator, a Q factor over 5000 was realized under normal incidence of a focused Gaussian beam, which is the highest in the LNOI platform. Using a device with a moderate Q factor (around 2000) and stronger optical field confinement, the SHG intensity was enhanced by over 1200 times under a pump power density of 1.92 MW/cm^2, leading to a normalized conversion efficiency of 2.03×10^{-5} cm^2/GW.

A schematic of the proposed structure is shown in Fig. 1(a). The GMR resonator is fabricated on a LNOI wafer, which is composed of a 500-nm-thick x-cut LN thin film, a 3-μm-thick SiO_2 buffer layer, and a 500-μm-thick quartz substrate. The GMR resonator is composed of the center grating coupler (GC) and two side DBRs. The one-dimensional GC supports GMR and acts as a free space coupler. The length of the GC is only 11 periods, which is chosen for a good match with a small incident spot. Two 130-period side DBRs are used to block light from lateral leakage. The whole structure is arranged in the y axis. The length of the grooves L is 30 μm. Phase shift (PS) regions are employed for phase matching between GC and DBR regions, which could be used to adjust the resonant wavelength and strength of resonance. Such a heterostructure cavity is also referred to as a cavity-resonator-integrated guided-mode resonance filter [41,42]. Figure 1(b) shows the cross-section view of the structure and a sketch of the nonlinear frequency conversion from fundamental harmonic (FH) pump to SHG signal beam. A focused z-polarized FH pump is back illuminated on the GC region, and the SHG signal is collected from the front. The period of the DBR a_1 is set as 410 nm, corresponding to a photonic band gap around 1550 nm. On the other hand, the period of the GC a_2 is set as 815 nm, to ensure the resonant wavelength around 1550 nm. The etching depth h of the GMR resonator is 100 nm. Widths of the etched grooves w are kept the same in the GC and DBR regions, which are set as 150 nm. The angle of the groove sidewall is 25° with respect to the surface normal.

The resonance polarization is designed as z polarized to utilize the maximum nonlinear coefficient tensor component d_{33} of LN. A finite difference time domain (FDTD) method is used to characterize the field localization and enhancement effect of the GMR resonator with z-polarized incidence. Primarily, photonic band structures of an infinite GC and DBR are calculated and shown in Figs. 1(c) and 1(d), respectively. Dispersion of the GMR shows a monotonic blueshift as the wave vector increases. Near the Γ point, it falls into the band gap of the DBR; thus, the electromagnetic field will be confined within the GC region. Figure 1(e) shows the calculated electric field intensity distribution of the whole resonator along the x-y plane at 1546.5 nm, using a PS width of $g = 560$ nm. An 8-μm-diameter Gaussian beam is used to excite the resonance at normal incidence. Because of the high-index contrast with

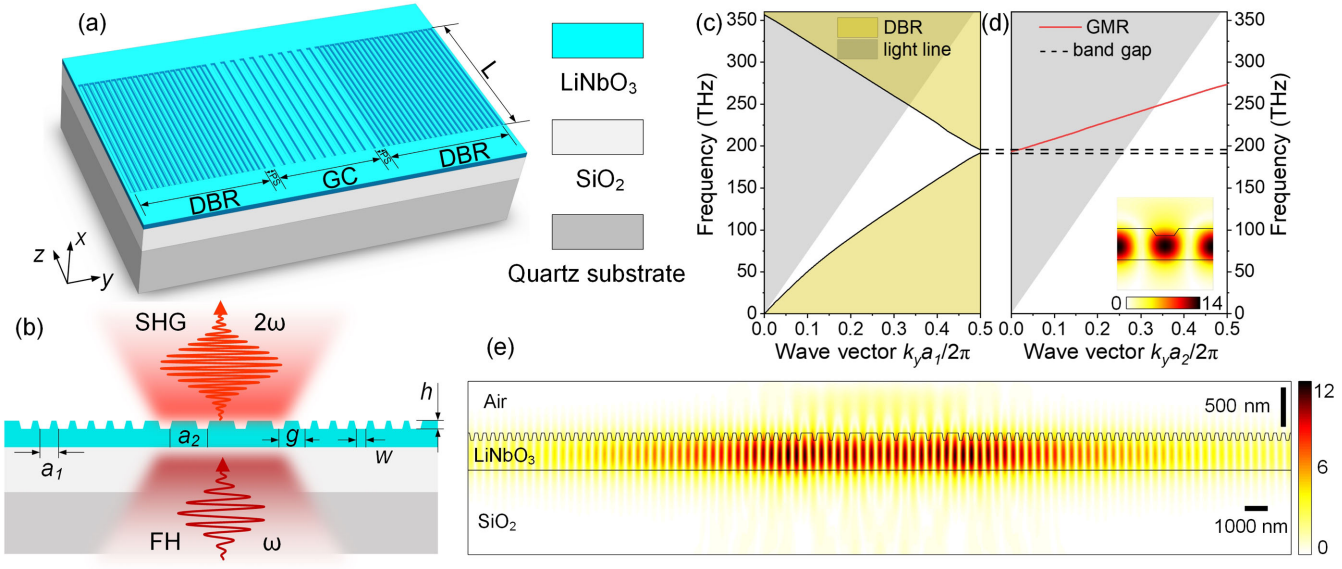

FIG. 1. (a) Schematic of the proposed LNOI GMR resonator, consisting of the center coupling grating and side DBRs. (b) A sketch of the pump and SHG signal beams at the sample. (c) Calculated band structure of a one-dimensional DBR with lattice constant $a_1 = 405$ nm. (d) Dispersion property of the GMR in a one-dimensional photonic crystal with lattice constant $a_2 = 810$ nm. The inset shows the electric field profile of GMR in one unit cell at the Γ point. (e) Simulated electric field intensity distribution of the GMR.

SiO_2, the field is mostly confined in the LN layer with strongly enhanced intensity, while along the y axis, the field intensity decreases rapidly as it enters the DBR region. It is noted that the maximum field enhancement in the heterostructure cavity is slightly smaller than that of the pure GMR resonator, which is due to the imperfect phase match and light scattering at the PS regions.

To achieve strong optical resonance in the heterostructure cavity around 1550 nm, we fabricated a series of devices with different structural parameters. The width of the PS region g, period of the GC a_2 (DBR a_1), and duty cycle of the GC (DBR) are the main parameters considered for optimization of the device performances. For convenience, periods of the GC and DBR are changed simultaneously, such that the relative position between the resonant wavelength and photonic band gap stays almost the same. On the other hand, the width of the PS region is changed to adjust the resonant wavelength, while the band gap stays unchanged. Duty cycles of the GC and DBR are adjusted by changing the width of the etched grooves w.

Figure 2 shows the scanning electron microscopic (SEM) images of a fabricated device in top view and cross-sectional view. The whole structure was patterned via EBL using ARP 6200.11 positive resist, which was then transferred to the LN layer using ICP etching with Ar ions. The etching depth is around 100 nm, and the angle of the groove sidewall is about 25° with respect to the surface normal. As can be seen, the high quality of the fabricated device implies high performance of the resonator, as shown below.

We first characterized the optical resonance properties of the devices around FH using a commercially available supercontinuum fiber laser (details of the measurement setup are given in Supplemental Material [43]). Figures 3(a)–3(c) give the transmission spectra measured under pump light with designed polarization, and the result of other polarization can be found in Supplemental Material [43]. As shown in Fig. 3(a), the resonant wavelength changes almost linearly with the period of the GC, in a ratio of 2.64:1. As a_2 increases from 800 to 815 nm, a_1 increases from 395 to 410 nm simultaneously. The slight changes in the extinction ratio and linewidth are mainly due to the variation of matching between the GC and DBR regions. Generally, the extinction ratio and linewidth of the resonance peak are in inverse proportion. Figure 3(b) gives the evolution of the resonances as w changes. At the submicron scale, the etching speed of LN is strongly related to the feature size of devices, resulting in a smaller etching depth as w decreases. As a consequence, the resonant wavelength changes monotonically but nonlinearly. It is worth noticing that the linewidth of the resonance decreases as the groove width becomes smaller. At $w = 100$ nm, the linewidth of the resonance decreases to 0.35 nm, corresponding to a high Q factor of 4445. In the proposed heterostructure GMR resonator, the Q factor is determined by radiation loss, as material losses of SiO_2 and LN are negligible at near 1550 nm wavelengths. The radiation loss consists of light coupling at the GC region and undesired scattering loss at the PS region; the former is directly related to the size of etched grooves. Thus, a higher Q factor is achieved at small w with proper PS width. Evolution of the resonance as a function of g is shown in Fig. 3(c). In addition to adjusting the matching between GC and DBR regions, changing g will also change the length of the resonant cavity, leading to changed resonant wavelengths. The split of the resonance peaks in Fig. 3(c) is due to the fabrication imperfections. Correspondingly, FDTD calculations were performed at the same structure

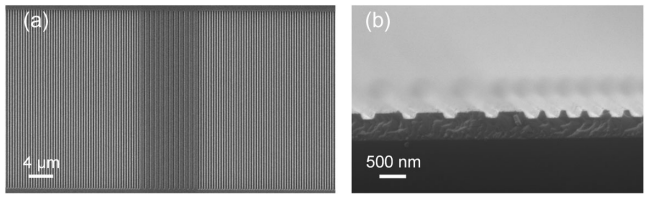

FIG. 2. (a) Top-view SEM image of the GMR resonator. (b) Cross-sectional SEM image of the resonator.

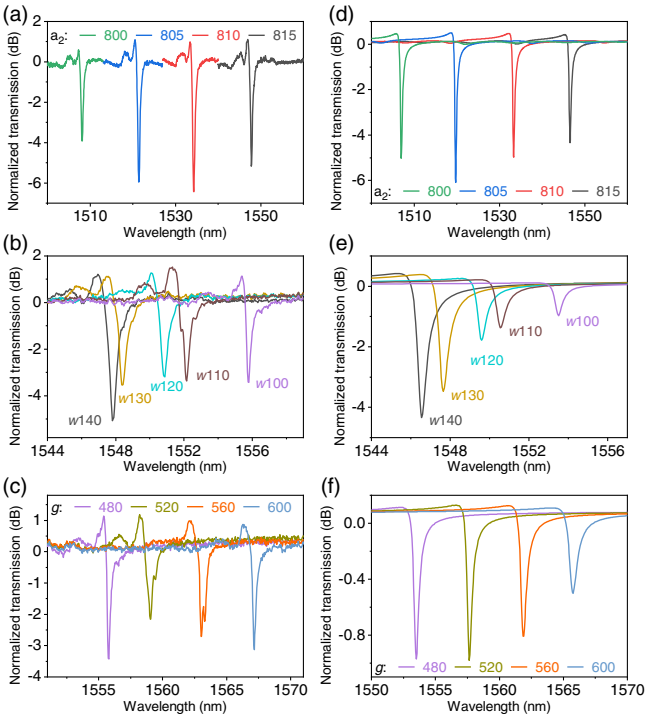

FIG. 3. (a)–(c) Experimentally measured transmission spectra as functions of (a) GC lattice constant a_2, (b) groove with w, and (c) PS width g. The structural parameters are arranged as (a) $w = 140$ nm, $g = 480$ nm; (b) $a_2 = 815$ nm, $g = 480$ nm; and (c) $w = 100$ nm, $a_2 = 815$ nm. (d)–(f) Corresponding FDTD-simulated transmission spectra as functions of a_2, w, and g. The spectra are normalized by experimentally measured and FDTD-simulated transmission spectra of the flat wafer, respectively.

parameters as fabricated devices, as can be seen in Figs. 3(e) and 3(f), showing good agreement between simulation and experiment results. The difference in resonant wavelength and extinction ratio mainly originates from fabrication imperfections.

By optimizing the structural parameters, strong resonance with an appropriate linewidth can be achieved at the designed wavelengths. The strongly enhanced local electromagnetic field will increase the optical nonlinear conversion efficiency. A nonlinear optical measurement system was set up to characterize such properties quantitatively, as schematically shown in Fig. 4(a). To investigate the enhancement of different resonant wavelength, we used a femtosecond pulsed laser with a central wavelength of 1560 nm and a spectral width of about 80 nm (T-light FC, MenloSystems) for pumping. The pump light was focused on the GMR resonator via an objective lens (50×, NA = 0.42), after being adjusted by the linear polarizer (LP) and half wave plate (HWP). The SHG signal light was collected by an objective lens with greater NA (60×, NA = 0.65) and further coupled into a multimode fiber.

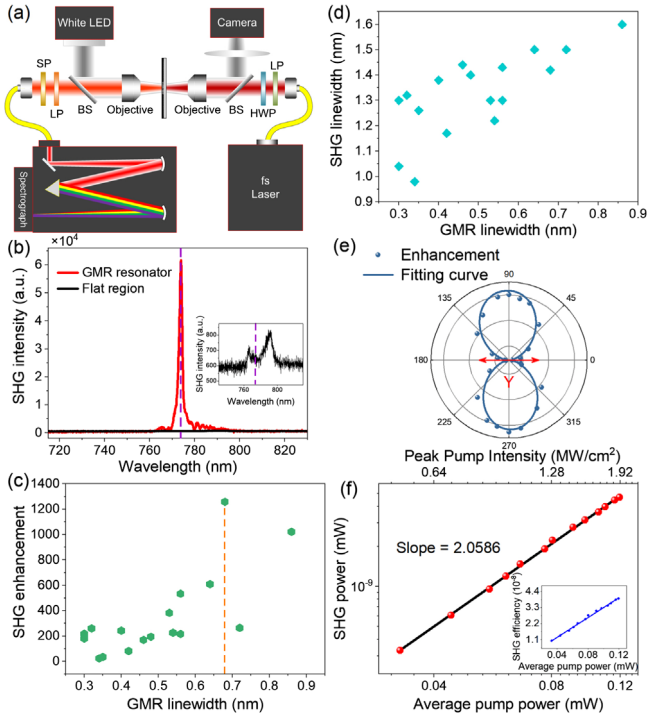

FIG. 4. (a) Schematic of the nonlinear experimental testing setup. (b) Measured SHG intensity of the GMR resonator and referential unpatterned wafer. The measured spectra have a background intensity of about 600 for the whole wavelength range, as shown in the inset. The resonance peak wavelength is marked by the dashed vertical line. (c),(d) Evolution of SHG enhancement and linewidth as a function of GMR linewidth. (e) Dependence of SHG enhancement on polarization of the pumping laser. (f) Power dependence of SHG in logarithmic scale, showing quadratic power scaling.

The collected signal light was then guided into the spectrometer (PYLON, Princeton) for measurement. An 860 nm short-pass filter and 650 nm long-pass filter were used to remove the pump light and third-harmonic generation; thus, only the SHG light was left for analysis.

Compared with the flat region of the LNOI wafer, strongly enhanced SHG was achieved at the resonant wavelengths of different devices. Especially, a highest enhancement of 1200 times is achieved at the structural parameters of $a_1 = 410$ nm, $a_2 = 815$ nm, $g = 480$ nm, and $w = 140$ nm, as shown in Fig. 4(b). The peak wavelength of SHG is 773.87 nm, as indicated by the dashed line. The corresponding SHG spectrum measured from the unpatterned wafer is given in the inset for comparison, showing a coincidence with the spectrum of pumping light (see details in Supplemental Material [43]). Such a large enhancement is due to the strong electric field confined in a small area, as the SHG intensity is proportional to the square of light intensity (the fourth power of electric field intensity). The measured second harmonic intensity spectra of devices with different structural parameters are also given in Supplemental Material [43].

Figure 4(c) shows the evolution of SHG enhancement as a function of the GMR linewidth, where the narrowest GMR linewidth is smaller than 0.3 nm, corresponding to a Q factor over 5000. It is worth noting that the largest enhancement is not achieved at the highest Q factor. The heterostructure cavity can be seen as a GMR resonator confined within a FP cavity. As the side DBRs are long enough to block in-plane lateral leakage, a higher Q factor can be achieved with decreased radiation loss of the GMR resonator. However, in the proposed design, the radiation loss is minimized with smaller etching depth, which will also weaken the confinement of side DBRs, leading to a longer penetration of the EM field into the DBR region (analogy to Fig. S7 in Supplemental Material [43]). As a result, weakened lateral confinement of DBRs could reduce the local field enhancement and, thus, the SHG enhancement. On the other hand, the overlap between mode profile and the pump light also becomes smaller with a higher Q factor, leading to smaller coupling efficiency (extinction ratio of the transmission spectrum). Therefore, the dependence of the measured SHG enhancement on the Q factor is not simple monotonic but needs to be properly chosen to balance the local field enhancement (determined by radiation loss and DBR confinement) and coupling efficiency of the pump light, since the efficiencies were calculated through the overall pump power. As shown in Fig. 4(c), a best result is achieved at a moderate Q factor. Figure 4(d) shows the evolution of GMR linewidth and the corresponding SHG linewidth, exhibiting an approximate linear relation.

Since the GMR resonator depends on the polarization of the pumping laser, the enhancement is supposed to have the same polarization dependence. We rotated the HWP and

measured SHG signal from GMR resonator and flat region with varied pump polarization, respectively. The enhancement factor could be calculated accordingly and is given in Fig. 4(e), showing a maximal value when the pumping light is z polarized. A good agreement between the experimental data and the fitted sine curve is found, which further reveals the links between the enhanced SHG and the GMR resonator structure.

To quantitatively calculate the nonlinear conversion efficiency of our structure, the pump light was filtered by a fiber filter with a central wavelength of 1547.72 nm and a spectral width of 5 nm. According to the Fourier optics, the bandwidth of the pulse in the time domain is inversely proportional to that in the frequency domain; thus, the new pulse width can be calculated as

$$\tau_{\mathrm{new}} = 90 \times 10^{-3} \times 80/5 \text{ ps} = 1.44 \text{ ps}.$$

The collected SHG light was imported into a photon counting module (PerkinElmer, SPCM-AQRH-15-FC) to measure the number of SHG photons and calculate the SHG power through $E = N \times \hbar c/\lambda$, in which N is the measured photon number, $\hbar$ is the Planck constant, c is the speed of light, and λ is the wavelength of SHG light. The measured power dependence of the SHG signal for structure in Fig. 4(b) is shown in Fig. 4(f). The unambiguous linear trend with a slope of ~2 in the log plot indicates the characteristic squared relationship between the SHG signal power and the average pumping power. The measured average power-dependent nonlinear conversion efficiency is shown in the insets. In our experiment, SH conversion efficiency of 3.92×10^{-8} is achieved with the averaged pump power of 0.12 mW, corresponding to a peak intensity of 1.92 $\mathrm{MW/cm^2}$ and an energy fluence of 2.77×10^{-6} $\mathrm{J/cm^2}$ per pulse.

It is known that the SH conversion efficiency is proportional to the intensity of pulses with fundamental frequency. Therefore, we defined a normalized conversion efficiency to theoretically quantify the SHG process as

$$\eta_{\mathrm{Norm}} = P^{\mathrm{SH}}_{\mathrm{avg}}/(P^{F}_{\mathrm{avg}} \times I^{F}_{\mathrm{peak}}) = \eta/I^{F}_{\mathrm{peak}}.$$

Here, η is the SH conversion efficiency, and I^{F}_{peak} is the pump peak intensity. This normalized efficiency is independent of pump intensity and could be regarded as a consistent and comparable parameter with other structure. Following this, the normalized efficiency of the GMR resonator is calculated as 2.03×10^{-5} $\mathrm{cm^2/GW}$. We compared our work with other special structures focusing on the enhancement of SHG in LN thin films and showed the results in Supplemental Material [43]. It can be seen that the proposed GMR resonator here achieves the highest enhancement and normalized conversion efficiency in experiments so far.

In summary, we have experimentally demonstrated record high Q-factor GMR resonators on a 500-nm-thick LNOI wafer. The localized and strongly enhanced electromagnetic field in the GC region of the resonator is utilized to boost the SHG efficiency. Over 1200 times enhancement of SHG intensity was realized under normal incidence of the femtosecond laser, leading to a high normalized conversion efficiency as large as 2.03×10^{-5} $\mathrm{cm^2/GW}$ at a pump intensity of 0.05 $\mathrm{GW/cm^2}$. Our results exhibit the potential of high-Q LNOI devices and pave the way for numerous on-chip photonic nonlinear conversion devices and systems in the LNOI platform.

This research was supported by National Key Research and Development Program of China (No. 2019YFB2203800), National Natural Science Foundation of China (NSFC) (No. 61590932, No. 61835008, No. 11774333, No. 62061160487, No. 61905079, and No. 61905084), the Anhui Initiative in Quantum Information Technologies (No. AHY130300), the Strategic Priority Research Program of the Chinese Academy of Sciences (No. XDB24030601), the National key R&D Program (No. 2016YFA0301700), and the Fundamental Research Funds for the Central Universities. We thank the Center of Optoelectronic Micro&Nano Fabrication and Characterizing Facility of WNLO for the facility support. This work is partially carried out at the USTC Center for Micro and Fabrication.

*These authors contributed equally to this work.
†renxf@ustc.edu.cn
‡jsxia@hust.edu.cn

[1] R. Weis and T. Gaylord, Appl. Phys. A **37**, 191 (1985).
[2] L. Arizmendi, Phys. Status Solidi (a) **201**, 253 (2004).
[3] E. L. Wooten, K. M. Kissa, A. Yi-Yan, E. J. Murphy, D. A. Lafaw, P. F. Hallemeier, D. Maack, D. V. Attanasio, D. J. Fritz, G. J. McBrien, and D. E. Bossi, IEEE J. Sel. Topics Quant. Electron. **6**, 69 (2000).
[4] A. Guarino, G. Poberaj, D. Rezzonico, R. Degl'Innocenti, and P. Günter, Nat. Photonics **1**, 407 (2007).
[5] W. Sohler, H. Hu, R. Ricken, V. Quiring, C. Vannahme, H. Herrmann, D. Büchter, S. Reza, W. Grundkötter, S. Orlov, H. Suche, R. Nouroozi, and Y. Min, Opt. Photonics News **19**, 24 (2008).
[6] G. Poberaj, H. Hu, W. Sohler, and P. Guenter, Laser Photonics Rev. **6**, 488 (2012).
[7] A. Boes, B. Corcoran, L. Chang, J. Bowers, and A. Mitchell, Laser Photonics Rev. **12**, 1700256 (2018).
[8] Y. Qi and Y. Li, Nanophotonics **9**, 1287 (2020).
[9] C. Wang, M. Zhang, X. Chen, M. Bertrand, A. Shams-Ansari, S. Chandrasekhar, P. Winzer, and M. Lončar, Nature (London) **562**, 101 (2018).
[10] M. He, M. Xu, Y. Ren, J. Jian, Z. Ruan, Y. Xu, S. Gao, S. Sun, X. Wen, L. Zhou, L. Liu, C. Guo, H. Chen, S. Yu, L. Liu, and X. Cai, Nat. Photonics **13**, 359 (2019).
[11] M. Xu, M. He, H. Zhang, J. Jian, Y. Pan, X. Liu, L. Chen, X. Meng, H. Chen, Z. Li, X. Xiao, S. Yu, S. Yu, and X. Cai, Nat. Commun. **11**, 3911 (2020).
[12] C. Wang, M. Zhang, B. Stern, M. Lipson, and M. Lončar, Opt. Express **26**, 1547 (2018).

[13] J. Lu, J. B. Surya, X. Liu, A. W. Bruch, Z. Gong, Y. Xu, and H. X. Tang, Optica **6**, 1455 (2019).
[14] C. Wang, C. Langrock, A. Marandi, M. Jankowski, M. Zhang, B. Desiatov, M. M. Fejer, and M. Lončar, Optica **5**, 1438 (2018).
[15] Y. Niu, C. Lin, X. Liu, Y. Chen, X. Hu, Y. Zhang, X. Cai, Y. Gong, Z. Xie, and S. Zhu, Appl. Phys. Lett. **116**, 101104 (2020).
[16] M. Li, H. Liang, R. Luo, Y. He, and Q. Lin, Laser Photonics Rev. **13**, 1800228 (2019).
[17] H. Jiang, H. Liang, R. Luo, X. Chen, Y. Chen, and Q. Lin, Appl. Phys. Lett. **113**, 021104 (2018).
[18] M. Li, J. Ling, Y. He, U. A. Javid, S. Xue, and Q. Lin, Nat. Commun. **11**, 4123 (2020).
[19] J. Lin, N. Yao, Z. Hao, J. Zhang, W. Mao, M. Wang, W. Chu, R. Wu, Z. Fang, L. Qiao, W. Fang, F. Bo, and Y. Cheng, Phys. Rev. Lett. **122**, 173903 (2019).
[20] J. Wang, F. Bo, S. Wan, W. Li, F. Gao, J. Li, G. Zhang, and J. Xu, Opt. Express **23**, 23072 (2015).
[21] M. Zhang, C. Wang, R. Cheng, A. Shams-Ansari, and M. Lončar, Optica **4**, 1536 (2017).
[22] A. Pan, C. Hu, C. Zeng, and J. Xia, Opt. Express **27**, 35659 (2019).
[23] M. Zhang, B. Buscaino, C. Wang, A. Shams-Ansari, C. Reimer, R. Zhu, J. M. Kahn, and M. Lončar, Nature (London)**568**, 373 (2019).
[24] C. Wang, M. Zhang, M. Yu, R. Zhu, H. Hu, and M. Loncar, Nat. Commun. **10**, 978 (2019).
[25] C. Wang, X. Xiong, N. Andrade, V. Venkataraman, X. F. Ren, G. C. Guo, and M. Lončar, Opt. Express **25**, 6963 (2017).
[26] C. Wang, Z. Li, M. H. Kim, X. Xiong, X. F. Ren, G. C. Guo, N. Yu, and M. Lončar, Nat. Commun. **8**, 2098 (2017).
[27] R. Luo, Y. He, H. Liang, M. Li, and Q. Lin, Optica **5**, 1006 (2018).
[28] Z. Hao, J. Wang, S. Ma, W. Mao, F. Bo, F. Gao, G. Zhang, and J. Xu, Photonics Res. **5**, 623 (2017).
[29] X. Ye, S. Liu, Y. Chen, Y. Zheng, and X. Chen, Opt. Lett. **45**, 523 (2020).
[30] J. Y. Chen, Y. M. Sua, Z. h. Ma, C. Tang, Z. Li, and Y. P. Huang, OSA Continuum **2**, 2914 (2019).
[31] L. Carletti, C. Li, J. Sautter, I. Staude, C. De Angelis, T. Li, and D. N. Neshev, Opt. Express **27**, 33391 (2019).
[32] A. Fedotova, M. Younesi, J. Sautter, A. Vaskin, F. J. F. Löchner, M. Steinert, R. Geiss, T. Pertsch, I. Staude, and F. Setzpfandt, Nano Lett. **20**, 8608 (2020).
[33] F. Renaud, A. Monmayrant, S. Calvez, O. Gauthier Lafaye, A. L. Fehrembach, and E. Popov, Opt. Lett. **44**, 5198 (2019).
[34] J. Ma, F. Xie, W. Chen, J. Chen, W. Wu, W. Liu, Y. Chen, W. Cai, M. Ren, and J. Xu, Laser Photonics Rev. **15**, 2000521 (2021).
[35] S. Wang and R. Magnusson, Appl. Opt. **32**, 2606 (1993).
[36] M. L. Brongersma, Y. Cui, and S. Fan, Nat. Mater. **13**, 451 (2014).
[37] Y.-C. Chang, A. V. Kildishev, E. E. Narimanov, and T. B. Norris, Phys. Rev. B **94**, 155430 (2016).
[38] J. Jin, X. Yin, L. Ni, M. Soljačić, B. Zhen, and C. Peng, Nature (London) **574**, 501 (2019).
[39] J. Lee, B. Zhen, S. L. Chua, W. Qiu, J. D. Joannopoulos, M. Soljačić, and O. Shapira, Phys. Rev. Lett. **109**, 067401 (2012).
[40] A. Cerjan, C. W. Hsu, and M. C. Rechtsman, Phys. Rev. Lett. **123**, 023902 (2019).
[41] G. Quaranta, G. Basset, O. J. F. Martin, and B. Gallinet, Laser Photonics Rev. **12**, 1800017 (2018).
[42] K. Kintaka, T. Majima, J. Inoue, K. Hatanaka, J. Nishii, and S. Ura, Opt. Express **20**, 1444 (2012).
[43] See Supplemental Material at http://link.aps.org/supplemental/10.1103/PhysRevLett.127.153901 for a comparison of SH conversion efficiency, which includes Refs. [31,32,34,44–46].
[44] K. H. Kim and W. S. Rim, ACS Photonics **5**, 4769 (2018).
[45] Y. Li, Z. Huang, Z. Sui, H. Chen, X. Zhang, W. Huang, and Z. Chen, Nanophotonics **9**, 3575 (2020).
[46] Z. Huang, M. Wang, Y. Li, J. Shang, K. Li, W. Qiu, J. Dong, H. Guan, and H. Lu, Nanotechnology **32**, 325207 (2021).]